Scholars' Mine

Spring 2014

Modelling of directed energy deposition processes

Xueyang Chen

Recommended Citation

MODELLING OF DIRECTED ENERGY DEPOSITION PROCESSES

by

XUEYANG CHEN

A THESIS

Presented to the Faculty of the Graduate School of the

MISSOURI UNIVERSITY OF SCIENCE AND TECHNOLOGY

In Partial Fulfillment of the Requirements for the Degree

MASTER OF SCIENCE IN MANUFACTURING ENGINEERING

2013

Approved by:
Dr. Frank Liou, Advisor
Dr. Joseph W. Newkirk
Dr. Frank Liu

PUBLICATION THESIS OPTION

This thesis consists of the following two articles that have been published, submitted for publication, or will be submitted for publication as follows:

Pages 3 – 19 were published in NAMRI/SME (The North American Manufacturing Research Institution of SME), Vol. 41, 2013.

Pages 20 – 47 are intended for submission to International Journal of Recent advances in Mechanical Engineering (IJMECH).

ABSTRACT

The laser additive manufacturing technique of laser deposition allows quick fabrication of fully-dense metallic components directly from Computer Aided Design (*CAD*) solid models. The applications of laser deposition include rapid prototyping, rapid tooling and part refurbishment. The development of an accurate predictive model for laser deposition is extremely complicated due to the multitude of process parameters and materials properties involved. In this work, a heat transfer and fluid flow model is developed.

In the heat transfer and fluid flow model, the governing equations for solid, liquid and gas phases in the calculation domain have been formulated using the continuum model. The free surface in the melt pool has been tracked by the Volume of Fluid (*VOF*) method. Surface tension was modeled by taking the Continuum Surface Force (*CSF*) model combined with a force-balance flow algorithm. Laser-powder interaction was modeled to account for the effects of laser power attenuation and powder temperature rise during the laser metal deposition process. Temperature-dependent thermal-physical material properties were considered in the numerical implementation.

The calculation domain is logically partitioned into smaller cells in 3D space. This makes the numerical implementation consume large amounts of computational resources as each cell is considered at each step of the implementation. This challenge has been addressed through the use of parallel computing by way of message passing interface. Simulations were performed and a comparison between the sequential and parallel implementations was also made.

ACKNOWLEDGMENTS

First and foremost, I would like to express my sincere gratitude to Dr. Frank Liou, my graduate advisor, for his continued patience, excellent guidance and encouragement during this research.

I would like to thank Dr. Joseph Newkirk for his advice and help in my research. His direction in my graduate work was invaluable and will be forever appreciated.

I would also like to thank my committee member, Dr. Frank Liu, for serving on my thesis committee and the various ways in which they assisted me in my study.

I would like to thank all members in LAMP lab, Zhiqiang Fan, Kenneth Fletcher, Todd Sparks, Heng Liu, Jingwei Zhang and Zhiyuan Wang, for making my research and study at Missouri S&T valuable and memorable.

Finally, I would like to thank my parents, for their untiring support and encouragement all these years. Their support and faith in me, has always encouraged me and helped me come out stronger from all the hard times. Love from family will always be strength to me.

TABLE OF CONTENTS

LIST OF ILLUSTRATIONS

LIST OF TABLES

SECTION

1. INTRODUCTION

Laser Metal Deposition (*LMD*) is a process which uses a laser beam to form a melt pool on a metallic substrate, into which powder is fed. The powder melts to form a deposit that is fusion bonded to the substrate. The required geometry is built up layer by layer. Both the laser and nozzle from which the powder is delivered are manipulated using a gantry system or robotic arm. *LMD* is used for a wide range of applications, including the generation of 3D free form structures and for cladding and repair applications. *LMD* also allows for near net shape manufacturing which dramatically reduces waste material and tooling costs.

LMD involves many process parameters, including total power and power intensity distribution of the energy source, travel speed, translation path, material feed rate and shielding gas pressure. Physical phenomena associated with laser deposition processes are complex, including melting/solidification and vaporization phase changes, free-surface flow with surface tension, heat and mass transfer, and moving heat source, and laser metal interaction. The variable process parameters together with the interacting physical phenomena involved in additive manufacturing complicate the development of process-property relationships and appropriate process control. Thus, an effective numerical modelling of the processing is very useful for assessing the impact of process parameters and predicting optimized conditions. However, such an implementation, when performed in a sequential manner, consumes a large amount of computation resources. As such, it is necessary to re-implement it in a parallel fashion, so that it can be executed

on several separate processors. Parallel implementation requires a little rethinking of the code structure, but is in reasonably simple and effective in many cases. This is achieved using Message Passing Interface (*MPI*), a platform independent standard for that contains sets of routines and also available in Fortran, C and C++.standard.

MPI is a library specification for message-passing proposed as a standard by a broadly based committee of vendors, implementers, and users. It is a standardized and portable message-passing system designed by a group of researchers from academia and industry to function on a wide variety of parallel computers.

Multiple processes are started from the beginning and run, usually on different CPUs to completion. These processes do not have anything in common, and each has its own memory space. Any information exchange requires communication of data, for which *MPI* was designed.

For high performance on both massively parallel, it is best used if your code has a good potential to employ many processors independently with none sitting idle. It is also advantageous to have only relatively little communication being necessary between processes. Examples are numerical integration (where independent evaluations of the integrant can be done separately), Monte-Carlo, finite-difference and finite-element methods.

In this work, an implementation of the model, both sequential and parallel, is presented. Results from simulations that were performed with both implementation styles are also presented and a comparison between them is also done.

PAPER

I. NUMERICAL SIMULATION OF DILUTION IN LASER METAL DEPOSITION BY POWDER INJECTION

1. INTRODUCTION

Laser deposition is an additive manufacturing technique. The applications of this technique include coatings, rapid prototyping and tooling, and part refurbishment. As shown in Fig. 1, laser deposition uses a focused laser beam as a heat source to create a melt pool on an underlying substrate. Powder material is then injected into the melt pool through nozzles. The incoming powder is metallurgically bonded with the substrate upon solidification.

A primary objective of laser deposition is to achieve porosity free added layers with good bonding to the substrate and with low dilution of the added layer. Thus, dilution is among the major concerns for this technique. Dilution is an important parameter for the laser deposition process. It indexes the bonding between the added layer and the substrate, and the utilization efficiency for the laser power. This parameter shows the amount of powder material dilution as a result of mixing with the substrate material. As an index of the bonding quality, too much dilution is disadvantageous for minimizing the heat-affected zone (*HAZ*). Dilution η_d is defined as the ratio of molten bulk material of cross section A_b to the total molten cross section $A_b + A_c$ according to Kaplan [4] as Fig. 2 shows:

$$\eta_d = \frac{A_b}{A_b + A_c}$$

(1)

where A_c is the cross section of the difference between the molten bulk material and the total molten material. Dilution depth D_d is the depth of the molten bulk. High dilution indicates that too much laser power has been used to re-melt the substrate and overheating may occur while no dilution at all leads to poor bonding to the substrate and even lack of fusion. Many investigations have been done on substrate dilution during the past years [1-7]. Blake et al. explained how irregular powder flow rates make an effect on dilution of laser cladding processes. When the laser power and traverse speed is constant, the less powder fed to the melt pool, the greater the dilution. If more powder fed to the melt pool, there would have a significant reducing the energy at the substrate[8]. It is considered that the control of the process for a given level of dilution which is sufficient to establish metallurgical bonding but which minimizes dilution would be desirable. However, such control is difficult because dilution highly depends on the material properties and the varying process parameters. Laser metal deposition involves many process parameters, including total power and power intensity distribution of the energy source, travel speed, translation path, material feed rate and shielding gas pressure. Physical phenomena associated with laser deposition processes are complex, including melting/solidification and vaporization phase changes, free-surface flow with surface tension, heat and mass transfer, and moving heat source, and laser metal interaction. A predictive model revealing the relationship between dilution and the above process parameters and physical phenomena has not been developed. In this study, a comprehensive heat transfer and fluid flow model is used to predict dilution under

different process parameters. A coaxial diode laser deposition system, Laser Aided

Manufacturing Processes (*LAMP*), is considered for simulations and experiments.

Material of both powder and substrates is Ti-6Al-4V alloy, which is widely used in the

aerospace industry and especially suitable for laser processing, since Ti-6Al-4V is still

classified as one of the extremely difficult-to-machine materials using conventional

machining.
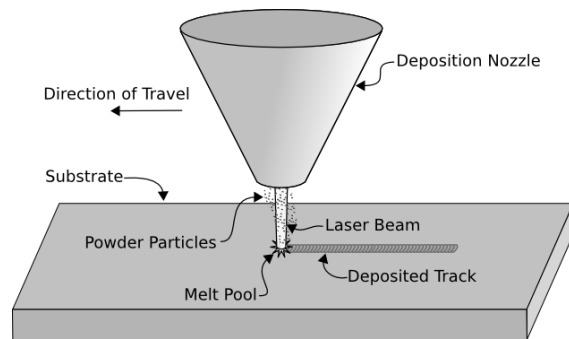
Figure 1. Schematic of a laser deposition system
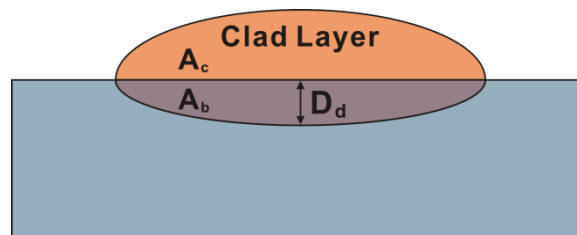
Figure 2. Schematic of the dilution and dilution depth definition

2. MATHEMATICAL MODEL

2.1 Governing Equations. Fig. 3 shows a schematic diagram of the calculation domain, including the substrate, melt pool, re-melted zone, deposited layer and part of the gas region. In this study the continuum model by Bennon and Incropera[9, 10] is adopted to derive the governing equations for melting and solidification with mushy zone. The assumptions include: (1) the fluid flow is Newtonian, incompressible, and laminar; (2) the solid and liquid phases in the mushy zone are in local thermal equilibrium; (3) the solid phase is rigid; and (4) isotropic permeability exists. For the system of interest, the conservation equations are summarized as follows:
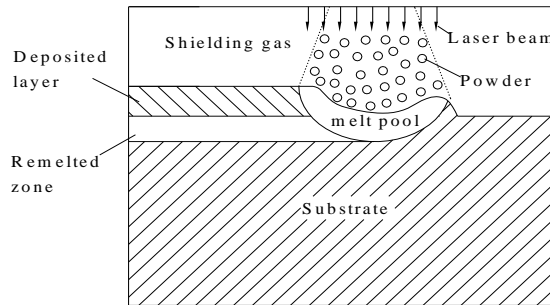
Figure 3. Schematic of the calculation domain

Continuity:

$$\frac{\partial \rho}{\partial t} + \nabla \cdot (\rho \vec{V}) = 0$$

(2)

Momentum

$$\frac{\partial}{\partial t}(\rho \bar{V}) + \nabla \cdot (\rho \bar{V} \bar{V}) = \nabla \cdot (\mu_l \frac{\rho}{\rho_l} \nabla \bar{V}) - \nabla p - \frac{\mu_l}{K} \frac{\rho}{\rho_l}(\bar{V} - \bar{V}_s) + \rho \bar{g} + S_1$$

(3)

Energy

$$\frac{\partial (\rho h)}{\partial t} + \nabla \cdot (\rho \bar{V} h) = \nabla \cdot (k \nabla T) - \nabla \cdot (\rho (h_l - h)(\bar{V} - \bar{V}_s)) + S_2$$

(4)

In eqns. (2)-(4), l represents the liquid and s represents the solid. The continuum density, specific heat, thermal conductivity, vector velocity and enthalpy are defined as follows

$$\rho = g_s \rho_s + g_l \rho_l, \quad c = f_s c_s + f_l c_l, \quad k = g_s k_s + g_l k_l, \quad \bar{V} = f_s \bar{V}_s + f_l \bar{V}_l, \quad h = f_s h_s + f_l h_l$$

(5)

The liquid fraction temperature relationship for Ti-6Al-4V is given by:

$$g_l = \begin{cases} 0 & \text{if } T < T_s \\ \dfrac{T - T_s}{T_l - T_s} & \text{if } T_s \leq T \leq T_l \\ 1 & \text{if } T > T_l \end{cases}$$

(6)

The other volume and mass fractions are obtained by:

$$f_l = \frac{g_l \rho_l}{\rho}, \quad f_s = \frac{g_s \rho_s}{\rho}, \quad g_s + g_l = 1, \quad f_s = 1 - f_l$$

(7)

The phase enthalpy for the solid and the liquid can be expressed as:

$$h_s = \int_0^T c_s(T) dT, \quad h_l = \int_0^{T_s} c_s(T) dT + \int_{T_s}^T c_l(T) dT + L_m$$

(8)

where L_m is the latent heat of melting.

The assumption of a multiphase region permeability requires consideration of growth morphology specific to the alloy under consideration. Permeability, K, is given by Carman [11]:

$$K = \frac{g_l^3}{C(1-g_l)^2}$$

(9)

where the parameter C can be calculated from Kubo et al. [12]

$$C = \frac{180}{d^2}$$

(10)

d is the dendritic spacing and assumed to be a constant of the order of 10^{-2} cm. The S_1 and S_2 are source terms that will be defined below.

2.2 Tracking of the Free Surface. The solid/liquid interface is implicitly tracked by the conservation equations. In solid phase region and liquid phase region, the third term on the right-hand side of eqn. (2) vanishes. This is because in solid phase region $\vec{V} = \vec{V}_s = 0$ and in the liquid phase region K→∞ since $g_l = 1$. So this term is only valid in the mushy zone. The liquid/vapor interface, or the free surface of the melt pool, is very complex due to surface tension, thermocapillary force, and impaction of the powder injection. In this study, the Volume-Of-Fluid (VOF) method by Hirt et al.[13] is employed to track the evolution of the moving free surface of the melt pool. The melt pool configuration is defined in terms of a volume of fluid function, F(x,y,t), which satisfies the conservation equation:

$$\frac{\partial F}{\partial t} + (V \cdot \nabla)F = 0$$

(11)

The value of F in a computational cell equals to the fractional volume of fluid in the cell. The cells with unity F values means the cells are full of fluid, while the cells with zero F values means the cells contain no fluid. The cells with F values between unity and zero are identified as interface cells.

2.3 Formulation of Source Terms. The source term, $\mathbf{S_1}$, in the momentum equation is contributed by the interface forces acting on the free surface. In this study, the continuum surface force (*CSF*) model by Brackbill et al. [14] is used to reformulate the surface force. The source term $\mathbf{S_1}$ in eqn. (3) is formulated as:

$$S_1 = (\bar{n}\gamma\kappa + \nabla_s\gamma)\left|\nabla F\right|\frac{F}{\bar{F}}$$

(12)

where $\bar{n}$ is the surface normal vector and can be computed from the gradient of VOF function:

$$\bar{n} = \nabla F$$

(13)

∇_s is the gradient along a direction tangential to the interface, which is defined as:

$$\nabla_s = \nabla - \nabla_N = \nabla - \hat{n}(\hat{n}\cdot\nabla)$$

(14)

$\bar{F}$ is the averaged F value across the free surface. γ and κ represent surface tension coefficient and curvature, respectively. κ is given in Prakash et al. [15]:

$$\kappa = -(\nabla\cdot\hat{n}) = \frac{1}{\left|\bar{n}\right|}\left[\left(\frac{n}{\left|\bar{n}\right|}\cdot\nabla\right)\left|\bar{n}\right| - (\nabla\cdot\bar{n})\right]$$

(15)

The similar formulation is applied to the energy boundary condition at the free surface. Energy balance at the free surface satisfies the following equation:

$$k\frac{\partial T}{\partial n} = \frac{\eta(P_{laser} - P_{atten})}{\pi R^2} - h_c(T - T_\infty) - \varepsilon\sigma(T^4 - T_\infty^4) - \dot{m}_e L_v$$

(16)

where terms on the right-hand side are laser irradiation, convective heat loss, radiation heat loss and evaporation heat loss, respectively. P_{laser} is the power of laser beam, P_{atten} the power attenuated by the powder cloud, R the laser beam radius, η the laser absorption coefficient, h_c the convective coefficient, T_∞ the ambient temperature, ε the radiation

emissivity, σ is the Stefan-Boltzmann constant, $\dot{m}_e$ the evaporation mass flux and L_v the latent heat of evaporation. The laser energy distribution is assumed to be uniform. P_{atten} is calculated according to Frenk's et al. [16] with modifications. Thus, S_2 can be formulated as:

$$S_2 = \left[\frac{\eta(P_{laser} - P_{atten})}{\pi R^2} - h_c(T - T_\infty) - \varepsilon\sigma(T^4 - T_\infty^4) - \dot{m}_e L_v\right]|\nabla F|\frac{F}{\overline{\overline{F}}} \tag{17}$$

2.4 Boundary Conditions. The boundary conditions at the free surface have been combined in the governing equations by volume formulation in the source terms. The boundary conditions at the bottom, left and right wall satisfy the following equations:

$$k\frac{\partial T}{\partial n} = -h_c(T - T_\infty) \tag{18}$$

$$u = 0, v = 0 \tag{19}$$

In this study, only those powder particles that have been melted before they arrive on the substrate and those that fall into the melt pool will be utilized. The mass ratio of utilized powder to total powder is calculated according to Pinkerton and Li's model [17].

3. NUMERICAL SIMULATION AND EXPERIMENTS

The governing equations and all related supplemental equations and boundary conditions are solved through an iterative scheme, which is based on the SOLA-VOF algorithm by Nichols et al. [18]. In this scheme, staggered grids are employed where the temperatures, pressures and Volume of Fluid (*VOF)* function are located at the cell center and the velocities at the walls. The source terms in the momentum and energy equations are obtained at grid points that are located in the transition region.

The parameters for simulations are chosen based on the capability of our experimental facilities. Fig. 4, referred from [19], shows the simulated temperature, velocity and *VOF* function fields. It is convenient to compute dilution using *VOF* function, which helps visualize the melt pool clearly. A cell with a VOF value greater or equal to 0.5 is counted as a liquid cell. The melt pool will enter a "steady state" in terms of shape and dimensions. The dilution calculation is based on the average value of the transient data in a "steady state" of the melt pool. For each computational cell, the molten area can be calculated by multiplying the cross section of the whole cell by the value of F. Then the cross section of the molten part can be calculated by adding the cells of the molten area together according to the following equation:

$$A = \sum dx \times dy \times F \tag{20}$$

where dx is the cell length in x direction, dy is the cell length in y direction. The simulation results are under the simulating time t = 130 ms.
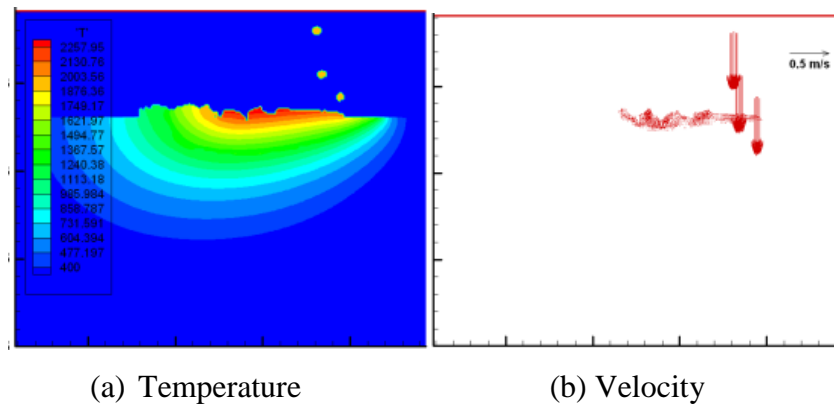
(a) Temperature (b) Velocity

Figure 4. Simulation results at t = 130 ms (laser power: 910W, travel speed: 20ipm, powder mass flow rate: 4.68g/min)
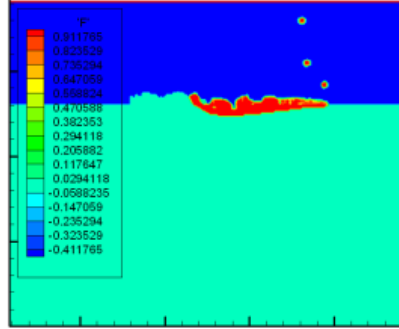
(c) Volume of fluid

Figure 4. Simulation results at t = 130 ms (laser power: 910W, travel speed: 20ipm, powder mass flow rate: 4.68g/min) (cont.)

The experiments were performed on the *LAMP* system shown in Fig. 5. The system consists of a diode laser, powder delivery unit, 5-axis CNC machine, and monitoring subsystem. The laser system used in the study was Nuvonyx ISL-1000M Laser Diode System with a maximum power of 1000 watts *CW*. The laser emits at 808 nm and operates in the continuous wave (*CW*) mode. The laser intensity distribution is uniform. To protect oxidization of Ti-6Al-V4, the system is covered in an environmental chamber to supply argon gas for titanium deposition. The laser spot diameter is 2.5 mm. The Ti-6Al-4V samples were irradiated using a laser beam with a beam spot diameter of 2.5 mm and laser powers (measured using a power meter) of 490-910W. The laser deposited samples were cut using a Wire-EDM machine. A SEM (Scanning Electron Microscope) line trace was used on each of the samples to determine the dilution of the clad layer. For the other aspects of the details, refer to[19].
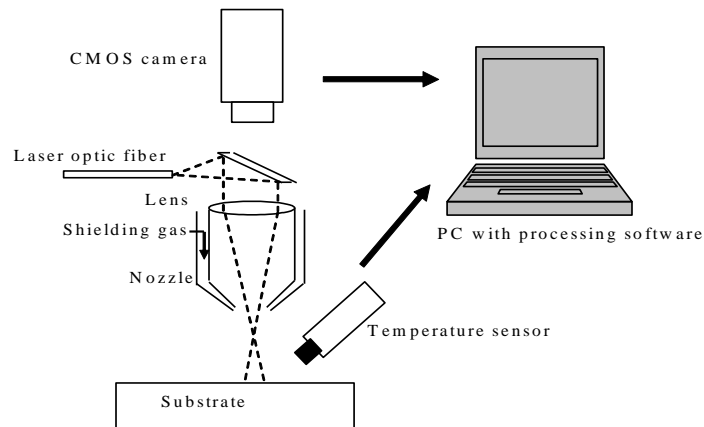
Figure 5. Schematic of experimental setup

Ti-6A1-4V powder has diameters between 40 μm and 140 μm. The substrates have dimensions of $2.5 \times 2.5 \times 0.4$ in. Laser powers, P_{laser}, are between 490 and 910W. A scanning electron microscope (*SEM*) line trace was used to determine the dilution. The deposited Ti-6Al-4V is of Widmansttaten structure. The substrate has a rolled equi-axed alpha + beta structure. Even though these two structures are easily distinguishable, the *HAZ* is large and has a martensitic structure that can be associated with it. Hence, a small quantity of tool steel in the order of 5% was mixed with Ti-6Al-4V. The presence of Cr in tool steel makes it easily identifiable by means of Energy Dispersive Spectroscopy (*EDS*) scans using *SEM*. Knowing the exact location of Cr in the substrate would provide the depth of the melt pool in the substrate to measure dilution.

A dilution analysis using *SEM* is shown in Fig.6, referred from [19]. Fig. 6 is referred from [19]. The upper part is the deposit. The lower part is the re-melt area, only part of it is shown in the images. In order to understand the effects of laser power, P_{laser},

travel speed, V_t, and powder mass flow rate, $\dot{m}$, on dilution, both simulation results and experimental results are shown in Figs. 7-9.
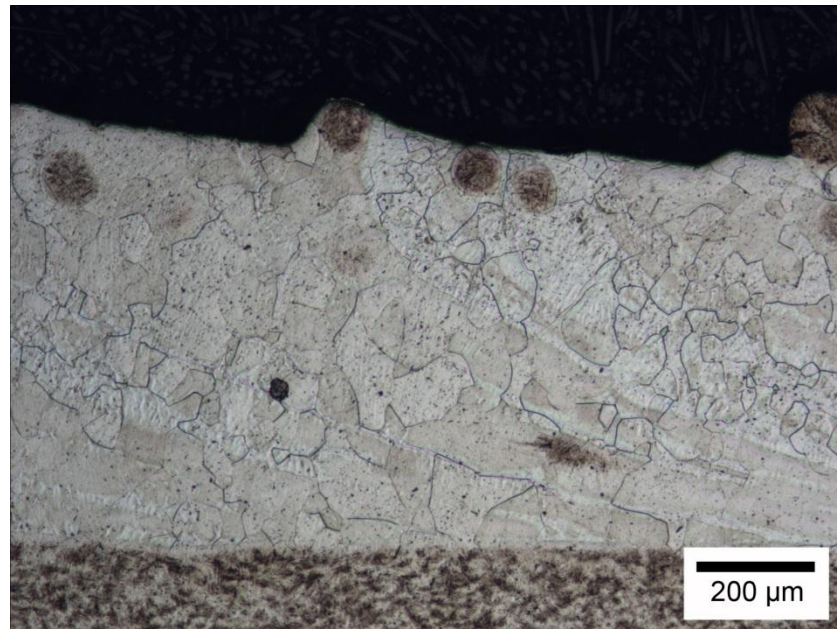
Figure 6. *SEM* picture of dilution analysis (Laser power: 910W, travel speed: 20ipm, powder mass flow rate: 6.7g/min))

(a) Dilution depth   (b) Dilution
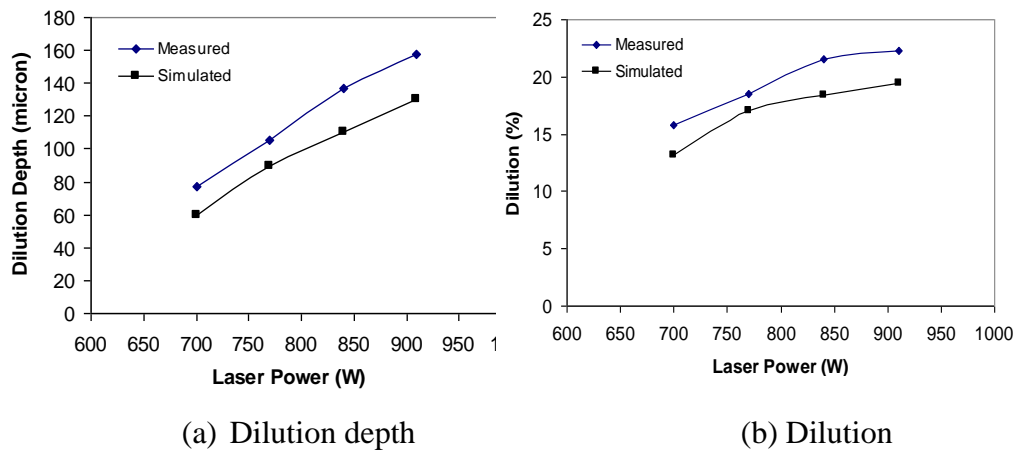
Figure 7. Dilution depth and dilution as a function of P_{laser} (V_t =20 ipm, $\dot{m}$= 4.68g/min)

(a) Dilution depth
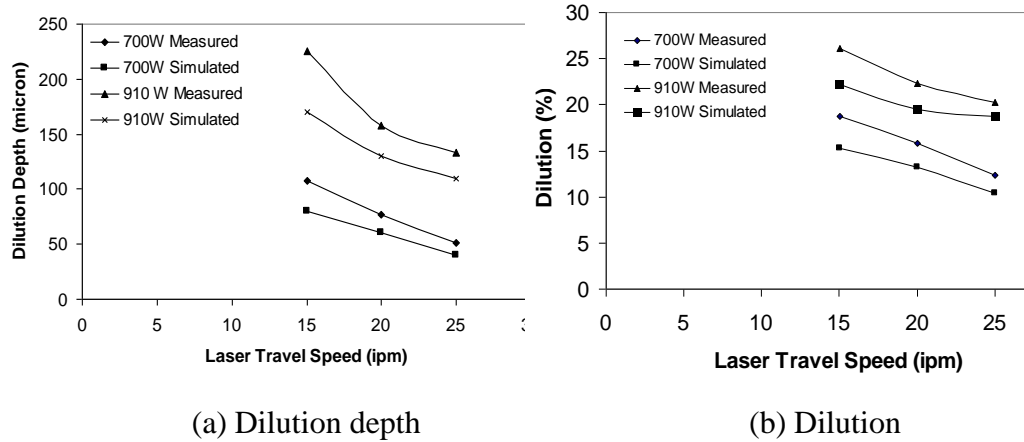
(b) Dilution

Figure 8. Dilution depth and dilution as a function of V_t ($\dot{m}$=4.68g/min)

(a) Dilution depth
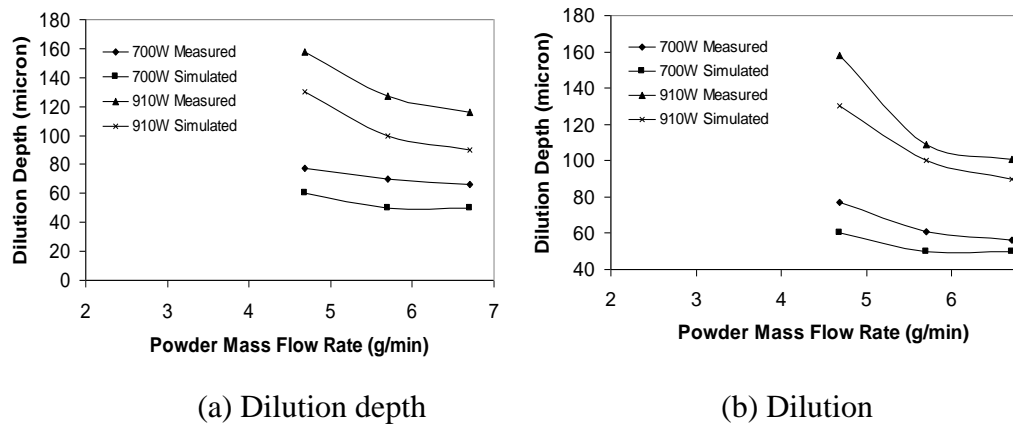
(b) Dilution

Figure 9. Dilution depth and dilution as a function of $\dot{m}$(V_t = 20 ipm)

4. DISCUSSION AND CONCLUSION

Dilution depth, depends on the energy absorbed by the substrate, given the specific material, the geometry of the substrate, laser beam spot size, and the beam profile. P_{laser} and V_t determine the total energy density potentially absorbed by the

substrate. $\dot{m}$ affects the energy actually absorbed by the substrate by the mechanism of power attenuation due to the powder cloud.

Dilution depends on both the dilution depth and the cross section area of the clad. The cross section area of the clad is determined by the clad height and the ripple of clad surface. From Figs. 7-8, it can be seen that an increase in the P_{laser} will increase the dilution depth. An increase in the V_t will decrease the dilution depth. It is clear that the dilution depth has a linear dependence on P_{laser} and V_t. This is easy to understand. As the P_{laser} increases, more power is available for melting the substrate. As V_t decreases, the laser material interaction time is extended. Because the powder encatchment efficiency, η_{pwd}, and thus the cross section area of the clad also increase with increased P_{laser} and decreased V_t, the dilution does not vary proportionally with the dilution depth.

It can be seen that an increase in $\dot{m}$ will decrease the dilution depth. But this effect is more significant at a lower level of $\dot{m}$. It is likely that at a lower level of $\dot{m}$, the effect of $\dot{m}$ on η_{pwd} is more significant. Also at a higher level of laser power, the effect of $\dot{m}$ on dilution depth is more significant. It is likely that at a higher level of P_{laser}, on one hand more power is attenuated given a constant attenuation ratio and more power is absorbed by the powder; on the other hand, the deposited material can decrease the temperature gradients more significantly.

From Fig. 7-9, we can see that the general trend between simulations and experiments is consistent. The errors are analysed using four aspects: (1) Mesh size of the numerical simulation is 10 μm, compared to the resolution of 1 μm for *SEM* measurement. (2) The *SEM* measurement of the dilution depth may bring about some errors. (3) Two-dimensional nature of the model intrinsically neglects heat transfer in the

third dimension. One can see that the errors between the simulated and measured dilution depths increase with increased laser power and decreased laser travel speed. This may be the case because a higher energy density heat and mass transfer in the third dimension is more significant. (4) The uncertainties of the material properties and the appropriateness of the sub-models are other possible sources of the errors.

The numerical simulation model can be used to predict the dilution in laser deposition both qualitatively and quantitatively. It is expected that a three dimensional model with finer mesh will improve the accuracy of prediction in dilution. Although this paper outlines the modelling of the same material in the cladding/deposition process, it will be a necessary step for modelling the dissimilar materials in the future.

5. ACKNOWLEDGEMENTS

6. RERERENCES

[1] Unocic, R.R. & DuPont, J.N., Composition control in the direct laser deposition process, *Metall. Mater. Trans*., **34B**, pp.439-445, 2003.

[2] Gedda, H., Kaplan, A. & Powell, J., Melt-solid interactions in laser cladding and laser casting, *Metall. Mater. Trans*., **36B**, pp. 683-689, 2005.

[3] Lei, T. C., Ouyang, J. H., Pei, Y. T. & Zhou, Y., Microstructure and sliding wear properties of laser clad TiN reinforced composite coating, *Surface Engineering*, **12**, pp.55-60, 1996.

[4] Kaplan, A. F. H. &Groboth, G., Process analysis of laser beam cladding, *Trans. ASME J. Manuf. Sci. Eng.*, **123**, pp. 609-614, 2001.

[5] Watkins, K. G., Achieving the potential of direct fabrication with lasers, Proc. of 3rd Int. Conf. on Laser Assisted Net Shaping, Erlangen, Germany, pp. 25-38, 2001.

[6] Griffith, M. L., Understanding thermal behaviour in the LENS process, *Materials and Design*, **20**, pp.107-113, 1999.

[7] Brice, C. A., Proc. of the Solid Freeform Fabrication Symposium, Austin, TX, pp. 369-374, 1999.

[8] Blake, A.G. &Eboo, G.M., State of the art laser hardfacing using dynamic powder feed technology, Conf. on the Laser vs. the Electron Beam in Welding, Cutting and Surface Treatment, Reno, Nevada, pp. 196-214, 1985.

[9] Bennon, W.D. &Incropera, F.P., A continuum model for momentum, heat and species transport in binary solid-liquid phase change systems-I. model formulation, Int. J. of Heat and Mass Transfer, **30**, pp. 2161-2170, 1987

[10] Bennon, W.D. &Incropera, F.P., A continuum model for momentum, heat and species transport in binary solid-liquid phase-change systems--II. Application to solidification in a rectangular cavity, Int. J. of Heat and Mass Transfer, **30**, pp.2171-2187, 1987.

[11] Carman, P.C., Fluid flow through granular beds, Trans. Institution Chem. Engrs., **15**, pp.150-166,1937.

[12] Kubo, K. &Pehlke, R. D., Mathematical modeling of porosity formation in solidification, Metallurgical Transactions, **16B**, pp. 359-365,1985.

[13] Hirt, C.W. & Nichols, B.D., Volume of fluid (VOF) method for the dynamics of free boundaries, J. of Comp. Physics, **39**, pp. 201-225,1981.

[14] Brackbill, J. U., Kothe, D. B. &Zemach, C., A continuum method for modeling surface tension, J. of Com. Physics, **100**, pp.335-354, 1992.

[15] Prakash, C. &Voller, V., On the numerical solution of continuum mixturemodel equations describing binary solid-liquid phase change, *NumericalHeat Transfer,* **15B**, pp.171-189, 1989.

[16] Frenk, A., Vandyoussefi, M., Wagniere, J., Zryd, A. &Kurz, W., Analysis of the laser-cladding process for stellite on steel,Metall. Mater. Trans., **28B**, pp. 501-508, 1997.

[17] Pinkerton, A. J. & Li, L., Modeling powder concentration distribution from a coaxial deposition nozzle for laser-based rapid tooling, *Trans. ASME J. Manuf. Sci. Eng.,***126**, pp. 33-41, 2004.

[18] B.D. Nichols, C.W. Hirt&R.S.Hotchkiss, SOLA-VOF: A solution algorithm for transient fluid flow with multiple free boundaries, LA-8355, Los Alamos National Laboratory, Los Alamos, New Mexico,1980.

[19] Z. Fan, A. Jambunathan, T. E. Sparks, J. Ruan, Y. Yang, Y. Bao, J. W. Newkirk, F. Liou, Proceedings of the Solid Freeform Fabrication Symposium, Austin, TX, pp. 532-545, 2006.

II. APPLICATION OF MESSAGE PASSING INTERFACE IN DIRECT METAL DEPOSITION

1. INTRODUCTION

Laser deposition is an extension of the laser cladding process for rapid prototyping of fully dense metal components. This laser additive manufacturing technique allows quick fabrication of fully-dense metallic components directly from Computer Aided Design (*CAD*) solid models. The applications include rapid prototyping, rapid tooling and part refurbishment. Laser metal deposition has an important advantage for these applications because it can produce near-net shape parts with little or no machining. Laser deposition uses a focused laser beam as a heat source to create a melt pool on an underlying substrate. Powder material is then injected into the melt pool through nozzles. The material studied is Ti-6Al-4V for both the substrate and powder.[1-11]

1.1 Modelling of Melting/Solidification Phase Change. The processes involve a melting/solidification phase change. Numerical modelling of the solidification of metal alloys is very challenging because a general solidification of metal alloys involves a so-called "mushy region" over which both solid and liquid coexist and the transport phenomena occur across a wide range of time and length scales.

To treat the effects of transport phenomena at the process-scale (~ 1 m), a macroscopic model needs to be adopted, where a representative volume element (*REV*) is selected to include a representative and uniform sampling of the mushy region such that

local scale solidification processes can be described by variables averaged over the *REV*. Based on the *REV* concept, governing equations for the mass, momentum, energy and species conservation at the process scale are developed and solved. Two main approaches have been used for the derivation and solution of the macroscopic conservation equations. One approach is the two-phase model, in which the two phases are treated as separate and separate volume-averaged conservation equations are derived for solid and liquid phases using a volume averaging technique. This approach gives the complete mathematical models for solidification developed today, which have the potential to build a strong linkage between physical phenomena occurring on macroscopic and microscopic scales. However, the numerical procedures of this model are fairly involved since two separate sets of conservation equations need to be solved and the interface between the two phases must be determined for each time step. This places a great demand on computational capabilities. In addition, the lack of information about the microscopic configuration at the solid-liquid interface is still a serious obstacle in the implementation of this model for practical applications. An alternative approach to the development of macroscopic conservation equations is the continuum model. This model uses the classical mixture theory to develop a single set of mass, momentum, energy and species conservation equations, which concurrently apply to the solid, liquid and mushy regions. The numerical procedures for this model are much simpler since the same equations are employed over the entire computational domain, thereby facilitating use of standard, single-phase *CFD* procedures. In this study, the continuum model is adopted to develop the governing equations.

1.2 Parallel Computing. The calculation domain is logically partitioned into smaller cells in 3D space. This makes the numerical implementation consume large amounts of computational resources as each cell is considered at each step of the implementation. As such, it is necessary to re-implement it in a parallel fashion, so that it can be executed on several separate processors. Parallel implementation requires a little rethinking of the code structure, but is in reasonably simple and effective in many cases. This is achieved using Message Passing Interface(*MPI*), a platform independent standard for that contains sets of routines and also available in Fortran, C and C++ standard.

MPI is a library specification for message-passing, proposed as a standard by a broadly based committee of vendors, implementers, and users. It is a standardized and portable message-passing system designed by a group of researchers from academia and industry to function on a wide variety of parallel computers.

Multiple processes are started from the beginning and run, usually on different CPUs to completion. These processes do not have anything in common, and each has its own memory space. Any information exchange requires communication of data, for which *MPI* was designed.

For high performance on both massively parallel machines and on workstation clusters, it is best used if the code has a good potential to employ many processors independently with none sitting idle. It is also advantageous to have only relatively little communication being necessary between processes. Examples are numerical integration (where independent evaluations of the integrant can be done separately), Monte-Carlo methods, finite-difference and finite-element methods (if the problem can be divided up into blocks of equal size with minimal communication).

2. MATHEMATICAL MODEL

2.1 Governing Equations. Figure 1 shows a schematic diagram of the laser deposition system. In the laser deposition process, melting and solidification cause the phase transformation at the solid/liquid interface. A mushy zone containing solid and liquid is formed. To track the solid/liquid interface evolution, in this study the continuum model developed by Bennon and Incropera[12, 13] is adopted, which is an extension of the classical mixture theory. The momentum equations are written for the mixture velocities, relying on the value of the permeability in each control volume to determine whether flow through porous mush is important in that control volume.
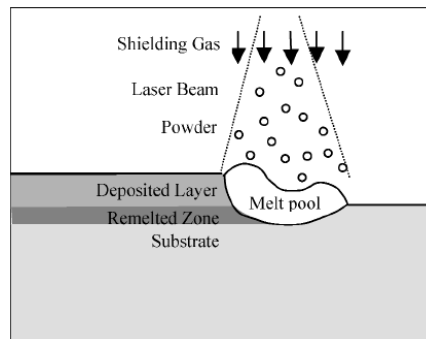

Figure 1. Schematic of the laser deposition system

For the system, a Newtonian, incompressible, laminar flow is assumed in the melt pool.

The conservation equations for mass, momentum and energy are summarized as follows:

Continuity

$$\frac{\partial \rho}{\partial t} + \nabla \cdot (\rho \bar{V}) = 0$$

(1)

Momentum

$$\frac{\partial}{\partial t}(\rho u) + \nabla \cdot (\rho \bar{V} u) = \nabla \cdot (\mu_l \frac{\rho}{\rho_l} \nabla u) - \frac{\partial p}{\partial x} - \frac{\mu_l}{K} \frac{\rho}{\rho_l}(u - u_s) + S_{\phi x}$$

(2)

$$\frac{\partial}{\partial t}(\rho v) + \nabla \cdot (\rho \bar{V} v) = \nabla \cdot (\mu_l \frac{\rho}{\rho_l} \nabla v) - \frac{\partial p}{\partial y} - \frac{\mu_l}{K} \frac{\rho}{\rho_l}(v - v_s) + \rho g + S_{\phi y}$$

(3)

$$\frac{\partial}{\partial t}(\rho w) + \nabla \cdot (\rho \bar{V} w) = \nabla \cdot (\mu_l \frac{\rho}{\rho_l} \nabla w) - \frac{\partial p}{\partial z} - \frac{\mu_l}{K} \frac{\rho}{\rho_l}(w - w_s) + S_{\phi z}$$

(4)

Energy

$$\frac{\partial(\rho h)}{\partial t} + \nabla \cdot (\rho \bar{V} h) = \nabla \cdot (k \nabla T) - \nabla \cdot (\rho (h_l - h)(\bar{V} - \bar{V}_s))$$

(5)

In equations (1)-(5), the continuum density, specific heat, thermal conductivity, vector velocity, and enthalpy are defined as follows:

$$\rho = g_s \rho_s + g_l \rho_l, \quad c = f_s c_s + f_l c_l, \quad k = g_s k_s + g_l k_l, \quad \bar{V} = f_s \bar{V}_s + f_l \bar{V}_l, \quad h = f_s h_s + f_l h_l$$
(6)

The volume fractions of liquid can be obtained from Swaminathan and Voller's general enthalpy method [14], although other relationships are possible [15]. Swaminathan and Voller summarized four possible enthalpy-temperature curves with different liquid fraction temperature relationships. In this work, both the deposit and the substrate materials are Ti-6Al-4V, for which Curve B is more appropriate where there is a linear evolution of the latent heat over the solidification range T_l–T_s. The liquid fraction temperature relationship for this type of enthalpy-temperature curve is given by:

$$g_l = \begin{cases} 0 & \text{if } T < T_s \\ \dfrac{T - T_s}{T_l - T_s} & \text{if } T_s \leq T \leq T_l \\ 1 & \text{if } T > T_l \end{cases}$$

(7)

The other volume and mass fractions are can be obtained by:

$$f_l = \frac{g_l \rho_l}{\rho}, \qquad f_s = \frac{g_s \rho_s}{\rho}, \qquad g_s + g_l = 1, \quad f_s = 1 - f_l \tag{8}$$

The phase enthalpy for the solid and the liquid can be expressed as:

$$h_s = \int_0^T c_s(T)\,dT, \qquad\qquad h_l = \int_0^{T_s} c_s(T)\,dT + \int_{T_s}^T c_l(T)\,dT + L_m \tag{9}$$

where L_m is the latent heat of melting.

The assumption of multiphase region permeability requires consideration of growth morphology specific to the alloy under consideration. The present study follows the approach suggested by Bennon and Incropera[12, 13], permeability, K, is assumed to vary with liquid volume fraction according to the Kozeny-Carman equation[16] derived from Darcy's law:

$$K = K_0 \frac{g_l^3}{(1 - g_l)^2} \tag{10}$$

where K_0 is a constant depending on the morphology and size of the dendrites in the mushy zone. The $S_{\phi x}$ and $S_{\phi y}$ in the momentum equations are source terms contributed by the interfacial forces such as thermocapillary force and surface tension.

2.2 Tracking of the Free Surface. The liquid/vapor interface, or the free surface of the melt pool, is very complex due to surface tension, thermocapillary force, and impaction of the powder injection. In this study, the Volume-Of-Fluid (*VOF*) method is employed to track the evolution of the moving free surface of the melt pool. The melt pool configuration is defined in terms of a volume of fluid function, *F(x,y,t)*, which represents the volume of fluid per unit volume and satisfies the conservation equation:

$$\frac{\partial F}{\partial t} + (V \cdot \nabla)F = 0 \tag{11}$$

2.3 Boundary Conditions. A free surface cell is subject to the following normal and tangential boundary condition:

Tangential stress balance:

$$\mu\left(\frac{\partial u_s}{\partial n} + \frac{\partial v_n}{\partial s}\right) = \frac{\partial \gamma}{\partial T} \cdot \frac{\partial T}{\partial s} \tag{12}$$

Normal stress balance:

$$p = p_v + \gamma \cdot \kappa \tag{13}$$

where u_s and v_n are the tangential and normal velocity component at the free surface. p_v is the vapor pressure in the gas region. γ and κ represent surface tension coefficient and curvature, respectively. κ is given in [15]:

$$\kappa = -(\nabla \cdot \bar{n}) = \frac{1}{|\bar{n}|}\left[\left(\frac{n}{|\bar{n}|} \cdot \nabla\right)|\bar{n}| - (\nabla \cdot \bar{n})\right] \tag{14}$$

where $\vec{n}$ is a normal vector of local free surface, which is a gradient of VOF function:

$$\bar{n} = \nabla F \tag{15}$$

2.4 Energy Balance. Energy balance at the free surface satisfies the following equation:

$$k\frac{\partial T}{\partial n} = \frac{\eta(P_{laser} - P_{atten})}{\pi R^2} - h_c(T - T_\infty) - \varepsilon\sigma(T^4 - T_\infty^4) - \dot{m}_e L_v \tag{16}$$

where terms on the right-hand side are laser irradiation, convective heat loss, radiation heat loss and evaporation heat loss, respectively. P_{laser} is the power of laser beam, P_{atten} is the power attenuated by the powder cloud, R is the laser beam radius, η is the laser absorption coefficient, which is measured by Sparks et al. [17]. The laser energy

distribution is assumed to be uniform, which is close to the actual conditions. P_{atten} is

calculated according to Frenk et al.'s model [18] with minor modification:

$$P_{atten} = P_{laser} \left[1 - \exp\left(- \frac{3 Q_{ext} \dot{m} l}{\pi \rho r_p D_{jet} v_p} \right) \right]$$

(17)

where $\dot{m}$ denotes the powder mass flow rate, l is the stand-off distance from the nozzle

exit to the substrate, ρ is powder density, r_p is the radius of the powder particle, D_{jet} is the

diameter of the powder jet, v_p is the powder injection velocity, and Q_{ext} is the extinction

coefficient. It is assumed that the extinction cross section is close to the actual

geometrical cross section, and Q_{ext} takes a value of unity.

In the evaporation term, $\dot{m}_e$ is the evaporation mass flux and L_v is the latent heat

of evaporation. According to Choi et al.'s "overall evaporation model" [19], $\dot{m}_e$ is of the

form:

$$\log \dot{m}_e = A + 6.1210 - \frac{18836}{T} - 0.5 \log T$$

(18)

where A is a constant dependent on the material.

2.5 Bottom and Side Wall Surfaces. The boundary conditions at the bottom, left

and right wall satisfy the following equations:

$$k \frac{\partial T}{\partial n} = - h_c (T - T_\infty)$$

(19)

$$u = 0 \qquad v = 0$$

(20)

Note that the radiation heat loss at these surfaces is neglected due to the fact that

the temperature differences at these surfaces are not large.

3. IMPLEMENTATION OF THE MATHEMATICAL MODEL

The mathematical model presented earlier has been implemented to evaluate its application. Two different implementations were performed; Sequential and Parallel implementations. Both implementations were performed using C++ under the 64-bit Ubuntu 13.04 on AMD FX™-8350 8 core processor.

3.1 Sequential Implementation. Finite difference and finite volume methods were used for spatial discretization of the governing equations to implement the sequential method numerically. Explicit Euler method was used for time discretization. A forward staggered, fixed grid, in which scalar quantities are located at the geometric center of the cell, was used whereas velocity components lie at the cell face centers. For discretization of the advection terms, the flux limiter scheme MUSCL (stands for Monotone Upstream-centered Schemes for Conservation Laws) [20] was applied to improve the accuracy of the upstream approximation and enforce the weak monotonicity in the advected quantity. The computational cycle can be described through the following iterative steps:

Equations (1) - (4) and the related boundary conditions are solved iteratively using a two-step projection method [21] first to obtain velocities and pressures. The second requires a solution of a Poisson equation for the pressure field,

$$\nabla \cdot [\frac{1}{\rho^n} \nabla p^{n+1}] = \frac{\nabla \cdot \vec{V}}{\delta t} \tag{21}$$

where ρ^n is the density from the old time step, p^{n+1} is the pressure to be solved at the new time step, and $\vec{v}$ is the temporary velocity field computed from the first step. The density retained inside the divergence operator in Equation (21) results in an extra term

proportional to $\nabla \rho$, which contributes to the pressure solution within the free surface

transition region where $\nabla \rho \neq 0$. The system of linear equations formulated from the

finite volume approximation of Equation (21) was solved with an Incomplete Cholesky

Conjugate Gradient (*ICCG*) solution technique [22]. Thermo-physical properties used in

this step are computed from the old temperature field.

Equation (5) is solved by a method [23] based on a finite volume discretization of

the enthalpy formulation of Equation (5). Once a new temperature field is obtained, the

thermo-physical properties are updated.

Equation (11) is solved using the PLIC-VOF [24-26] to obtain the updated free

surface, geometry of the melt pool and thermal field.

Advance to the next time step and return to step 1 until the desired process time is

reached.

3.2 Parallel Implementation. The sequential implementation was expensive

with respect to time and space complexity. The time complexity is upper bounded by the

number of iterations the solver needs to go through to converge during each time step.

This number at the area where the molten pool is formed is very high. For a 4mm x 1mm

x 2mm domain size, a grid of 200 x 50 x 100 (the numbers represent the number of

elements in the x, y and z directions respectively), it will take about 6.5 hours for

sequential simulation. The space complexity is also upper bounded by the number of 3D

variables that needs to be kept since the model employs a static mesh configuration. For

instance, for a grid of 1000 x 500 x 1000 (the numbers represent the number of elements

in the x, y and z directions respectively), the amount of memory needed is 87.8GB. In

order to alleviate these issues, it became necessary to re-implement the sequential code in

a parallel fashion. In this way, the parallel code can be executed on a cluster for better performance.

To accomplish the parallel implementation, a platform independent standard, Message Passing Interface (*MPI*), was employed. *MPI* is a library specification for message-passing, proposed as a standard by a broadly based committee of vendors, implementers, and users [27]. It is a standardized and portable message-passing system designed by a group of researchers from academia and industry to function on a wide variety of parallel computers. It consists of a set of functions, available in C++ and other programming languages, which when applied correctly, can achieve parallelization. *MPI* attempts to be practical, portable, efficient, and flexible [28]. Multiple processes are started from the beginning and run, usually on different processors (CPUs/nodes/cores), to completion. *MPI* uses distributed memory architecture. This means each processor has their own memory space and communication among processors is achieved through a network.

The parallel implementation begins by initializing the *MPI* interface with the *MPI_Init f*unction. *MPI_Comm_size* and *MPI_Comm_rank* set the number of processors and the presently running process respectively. It should be noted that processes are numbered from 0...n, where n = T_m-1 and T_m is the total number of processors used. Figure 2 shows how the above functions are called. The identifier *MPI_COMM_WORLD* is used to label a group of processes assigned to this task, called a "communicator".

```
void initMPI(int argc, char* argv[])
{
     MPI_Init(&argc, &argv);
     MPI_Comm_size(MPI_COMM_WORLD, &numMPINodes);
     MPI_Comm_rank(MPI_COMM_WORLD, &mpiRank);
}
```

Figure 2. C++ code snippet showing the *MPI* initialization

Next, the domain (a representation of the 3D static mesh consisting of the

substrate and void), is partitioned among the number of processors available. In the

implementation, the partitioning was done only in the x direction because that is the laser

travel direction. Figure 3 is an example of a domain partitioned among 5 processors. Each

partition is assigned to a processor. The assignment is performed such that the first

partition is assigned to the first processor, the second to the second processor, etc. For

instance, in Figure3, partition 1 is assigned to processor 0, partition 2 to processor 1,

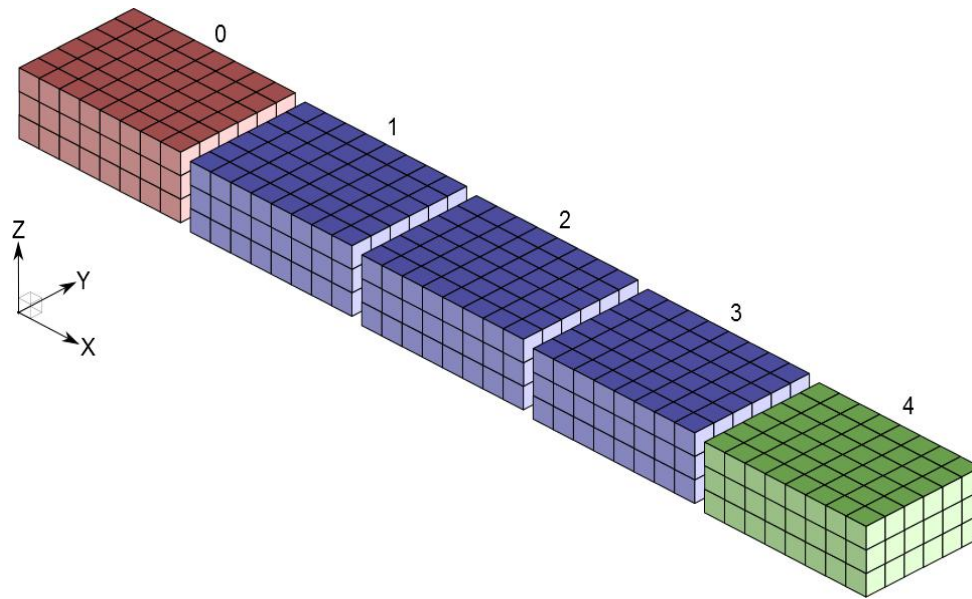partition 3 assigned to processor 2 and so on.

Figure 3. Domain partitions with their associated processor numbers

Based on an analysis performed on the sequential code, the partitions are
categorized into 3 main regions; *NODE_0*, *NODE_i*, and *NODE_n*. The leftmost and
rightmost partitions are placed in *NODE_0* and *NODE_n* categories respectively. All
other partitions are placed in *NODE_i* category. The categorization is mainly based on
how the code fragments in those partitions will be executed. Figure 4 shows the C++
code snippet to carry out this task. In the figure, *sliceN* is the total number of elements in
each partition, and *DIMX* is the total number of elements in the x direction. *imaxBeg* and
imaxEnd are the beginning and ending indices respectively for each partition.

```
sliceN=DIMX/numMPINodes;
if (mpiRank == 0)
{
     nodePos = NODE_0;
     imaxBeg=0; imaxEnd=sliceN+2;
}
elseif (mpiRank < numMPINodes-1)
{
     nodePos = NODE_i;
     imaxBeg=0; imaxEnd=sliceN+4;
}
elseif (mpiRank == numMPINodes-1)
{
     nodePos = NODE_n;
     imaxBeg=0; imaxEnd=sliceN+2;
}
```

Figure 4. C++ code snippet that deals with partitioning of the domain

The nature of the sequential implementation requires that each cell in the domain utilizes data from its neighboring cells. Owing to this, it is necessary for the processors in the parallel implementation to communicate with each other to exchange data. This is the final step in the parallel implementation in order to achieve parallelism of the sequential code. In order to achieve this in the partitioned domain, compatibility cells, which are shown in red, are added to each partition (see Figure 5). The compatibility cells basically hold data from nearby partition(s). For instance, compatibility cells added to partition 1 (processor 0), will hold left boundary data of partition 2 (processor 1) and compatibility cells added to partition 2 (processor 1) will hold data the right boundary data of partition 1 (processor 0) and the left boundary data of partition 3 (processor 2), as shown in Figure 5. In the same figure, ghost cells are added to the beginning and the end of the domain so that the finite difference derivative exists at the first and last cells.
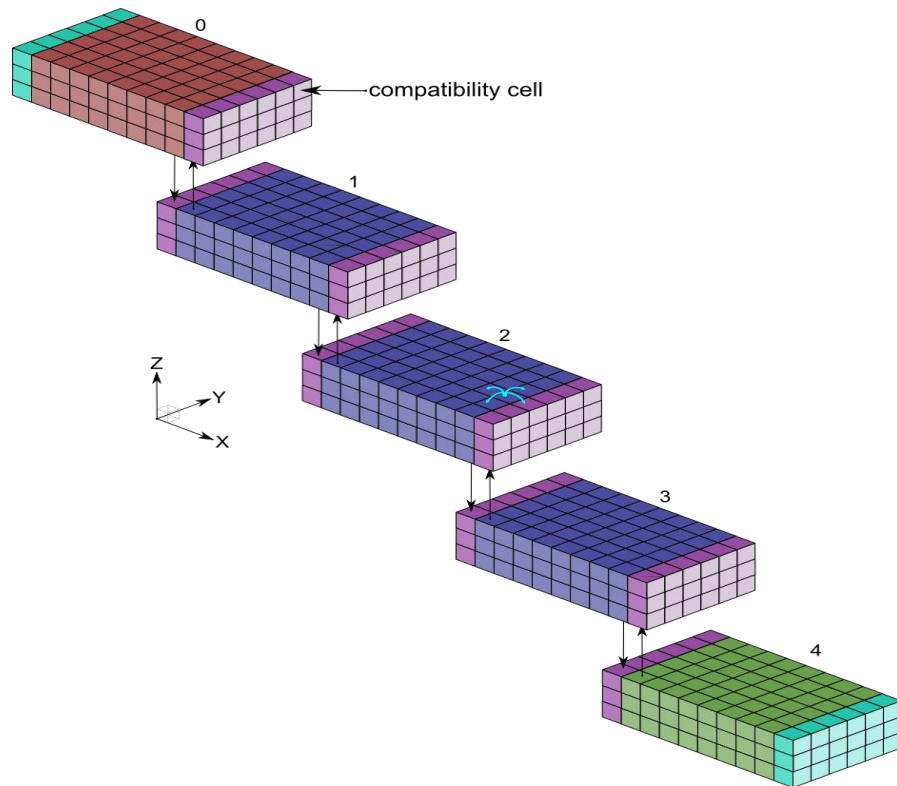
Figure 5. Domain partitions exchanging data among themselves

Two main *MPI* functions are used for the exchange of data among processors;

MPI_Barrier and *MPI_Sendrecv*. *MPI_Barrier* blocks until all processes in the

communicator have reached this function. The call to this function returns at any process

only after all group members have entered the call [29]. *MPI_Sendrecv* sends and receive

a message to and from other processor(s). It combines in one call the sending of a

message to one destination (processor) and the receiving of another message, from

another process [29]. A special value *MPI_PROC_NULL* can be used instead of a rank

wherever a source or a destination argument is required in a call [30]. Communication

with process *MPI_PROC_NULL* has no effect [30]. Figure 6 shows the code that

accomplishes the data exchange task. The code shows the areas where data is exchanged.

```
void sliceMove(float ***arr2move)
{
      int myLeft, myRight, istat;
      MPI_Status status;
      MPI_Barrier(MPI_COMM_WORLD);
      myRight = mpiRank + 1;
      if (myRight >= numMPINodes) myRight = MPI_PROC_NULL;
      myLeft = mpiRank - 1;
      if (myLeft < 0) myLeft = MPI_PROC_NULL;

      if ((mpiRank % 2) == 0) {
            if (mpiRank != numMPINodes-1) {/* exchange right */
                  if (mpiRank == 0) {
                        MPI_Sendrecv((void *)&arr2move[sliceN-1][0][0], DIMY*DIMZ, MPI_FLOAT, myRight, 0,
                              (void *)&arr2move[sliceN][0][0], DIMY*DIMZ, MPI_FLOAT, myRight, 0,
                              MPI_COMM_WORLD, &status); }
                  else {
                        MPI_Sendrecv((void *)&arr2move[sliceN+1][0][0], DIMY*DIMZ, MPI_FLOAT, myRight, 0,
                              (void *)&arr2move[sliceN+2][0][0], DIMY*DIMZ, MPI_FLOAT, myRight, 0,
                              MPI_COMM_WORLD, &status);}}}
      else  {
            if (mpiRank != 0){ /* exchange left */
                  MPI_Sendrecv((void *)&arr2move[2][0][0], DIMY*DIMZ, MPI_FLOAT, myLeft, 0,
                        (void *)&arr2move[1][0][0], DIMY*DIMZ, MPI_FLOAT, myLeft, 0,
                        MPI_COMM_WORLD, &status);}}

      MPI_Barrier(MPI_COMM_WORLD);

      if ((mpiRank % 2) == 1){ /* exchange right */
            if (mpiRank != numMPINodes-1) {
                  MPI_Sendrecv((void *)&arr2move[sliceN+1][0][0], DIMY*DIMZ, MPI_FLOAT, myRight, 1,
                        (void *)&arr2move[sliceN+2][0][0], DIMY*DIMZ, MPI_FLOAT, myRight, 1,
                        MPI_COMM_WORLD, &status);}}
      else {
            if (mpiRank != 0){ /* exchange left */
                  MPI_Sendrecv((void *)&arr2move[2][0][0], DIMY*DIMZ, MPI_FLOAT, myLeft, 1,
                        (void *)&arr2move[1][0][0], DIMY*DIMZ, MPI_FLOAT, myLeft, 1,
                        MPI_COMM_WORLD, &status);}}
      MPI_Barrier(MPI_COMM_WORLD);
}
```

Figure 6. C++ code snippet that deals with the exchange of data among processors

3.3 Simulation Parameters. The parameters for the simulation are chosen based

on the capability of our experimental facilities to compare the simulation results with the

experimental measurements. In this study, laser deposition processes by the *LAMP*

deposition system of Missouri S&T with a 400 W diode laser were modeled. A continuous wave diode laser with a 1 mm beam diameter is considered as the energy source. The laser intensity distribution is uniform. The laser absorption coefficient is measured by Sparks et al. [31]. The material properties for Ti-6Al-4V and the main process parameters are shown in Table 1.

Table 1. Material Properties for Ti-6Al-4V and Main Process Parameters

| Property	Symbol	Value
Melting temperature	T_m	1900.0K
Liquidus temperature	T_l	1923.0K
Solidus temperature	T_s	1877.0K
Evaporation temperature	T_v	3533.0K
Solid specific heat at constant pressure [32]	c_{ps}	$\begin{cases} 483.04 + 0.215T & T \leq 1268K \\ 412.7 + 0.1801T & 1268 < T \leq 1923 \end{cases} J/kg\ K$
Liquid specific heat at constant pressure [33]	c_{pl}	831.0 J/kg K
Thermal conductivity [32]	k	$\begin{cases} 1.2595 + 0.0157T & T \leq 1268K \\ 3.5127 + 0.0127T & 1268 < T \leq 1923 \quad W/m\ K \\ -12.752 + 0.024T & T > 1923 \end{cases}$
Solid density [33]	ρ_s	4420 – 0.154 (T – 298 K)
Liquid density [33]	ρ_l	3920 – 0.68 (T – 1923 K)
Latent heat of fusion [33]	L_m	2.86×10^5 J/kg
Latent heat of evaporation	L_v	9.83×10^6 J/kg
Dynamic viscosity	μ	3.25×10^{-3} N/m s (1923K) 3.03×10^{-3} (1973K) 2.66×10^{-3} (2073K) 2.36×10^{-3} (2173K)
Radiation emissivity [34]	ε	$0.1536 + 1.8377 \times 10^{-4}$ (T - 300.0 K)
Laser absorption coefficient [31]	η	0.4
Powder particle diameter	D_p	40-140 μm
Shielding gas pressure	P_g	5 psi
Ambient temperature	T_∞	300K
Convective coefficient	h_c	10 W/m^2 K

3.4 Simulation Results. With the parameters in Table 1, the laser deposition process was simulated using both the sequential and parallel implementations.

Figure 7 shows the simulation results of the temperature field and liquid volume fraction at time 0.008secs using the parallel implementation. Using the sequential implementation can get the same simulation results. As the laser move, we can see the temperature gradient. And the red part shows the melt pool.
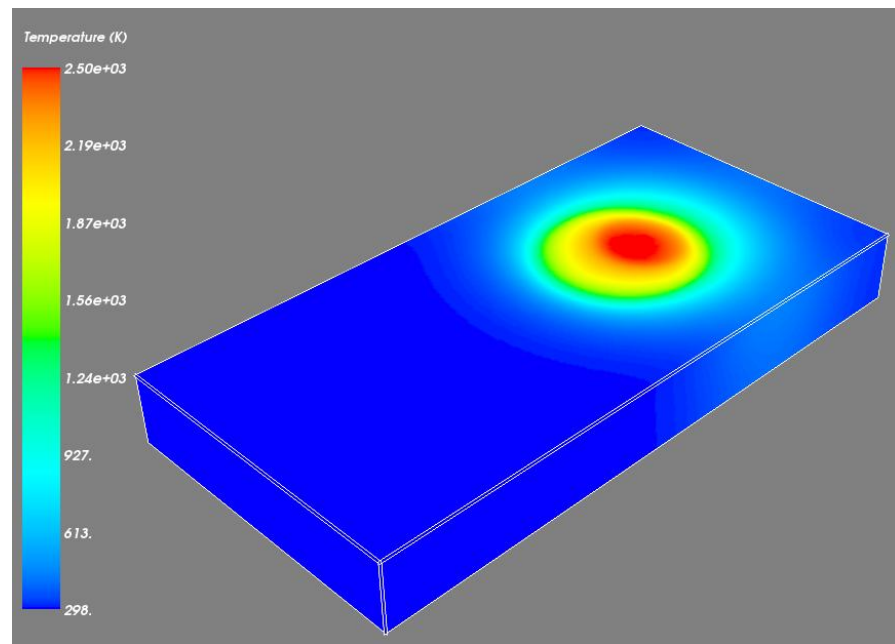
(a) Temperature field of the simulation at time 0.008secs

Figure 7. Temperature field and Liquid volume fraction of the simulation at time
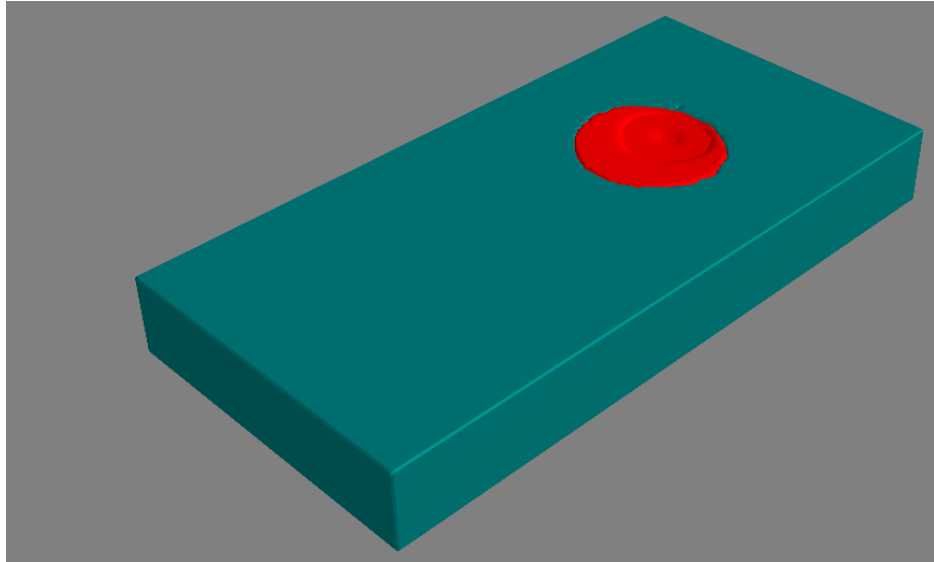
0.008secs

(b) Liquid volume fraction of the simulation at time 0.008secs

Figure 7. Temperature field and Liquid volume fraction of the simulation at time 0.008secs (cont.)

Other simulations were performed on 2mm x 0.5mm x 1mm, 4mm x 1mm x 2mm and 6mm x 1.5mm x 3mmdomain sizes, the grids of 100 x 25 x 50, 200 x 50 x 100 and 300 x 75 x 150 (the numbers represent the number of elements in the x, y and z directions respectively). The number of processors in the parallel implementation was varied from 2, 4, 6 and 8 for each grid. All the computation times was obtained under the same cycle number, 5000.Figure 8 shows a comparison of the computation times for different implementation methods used.
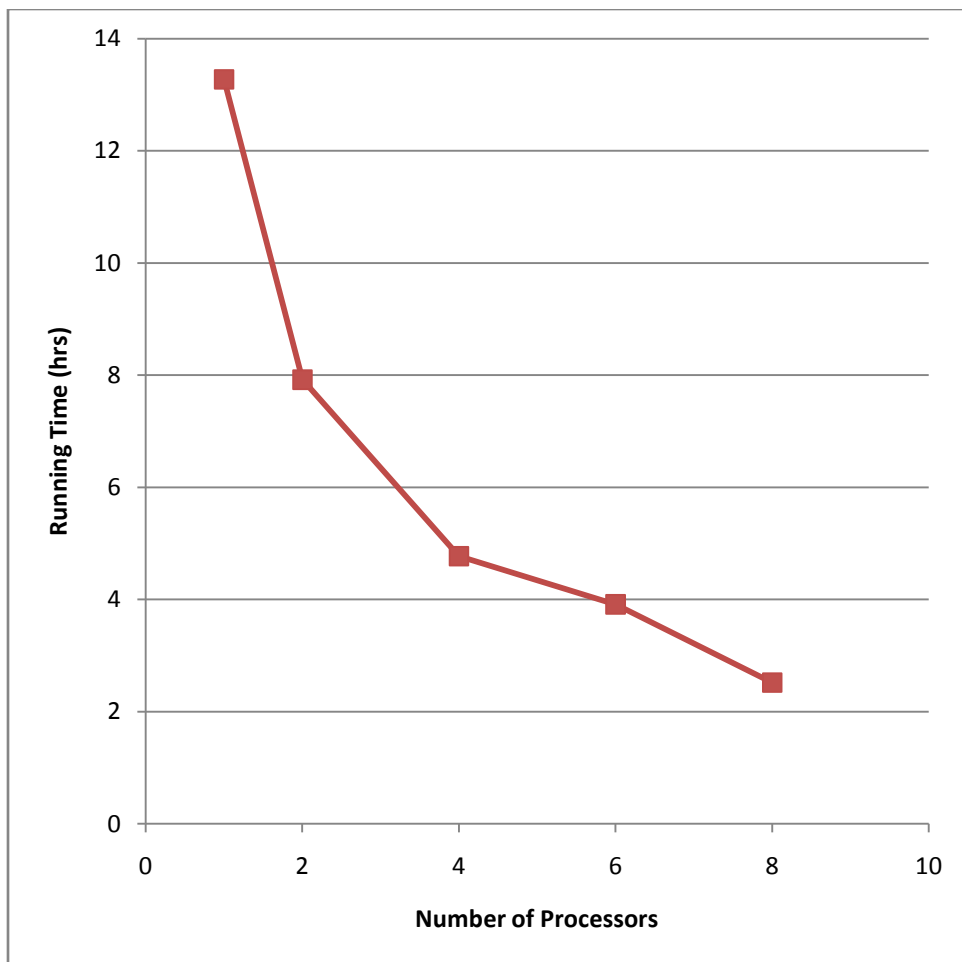
(a)the 300 x 75 x 150 grid

Figure 8. A comparison of the serial and parallel implementation using different number of processors on different grids
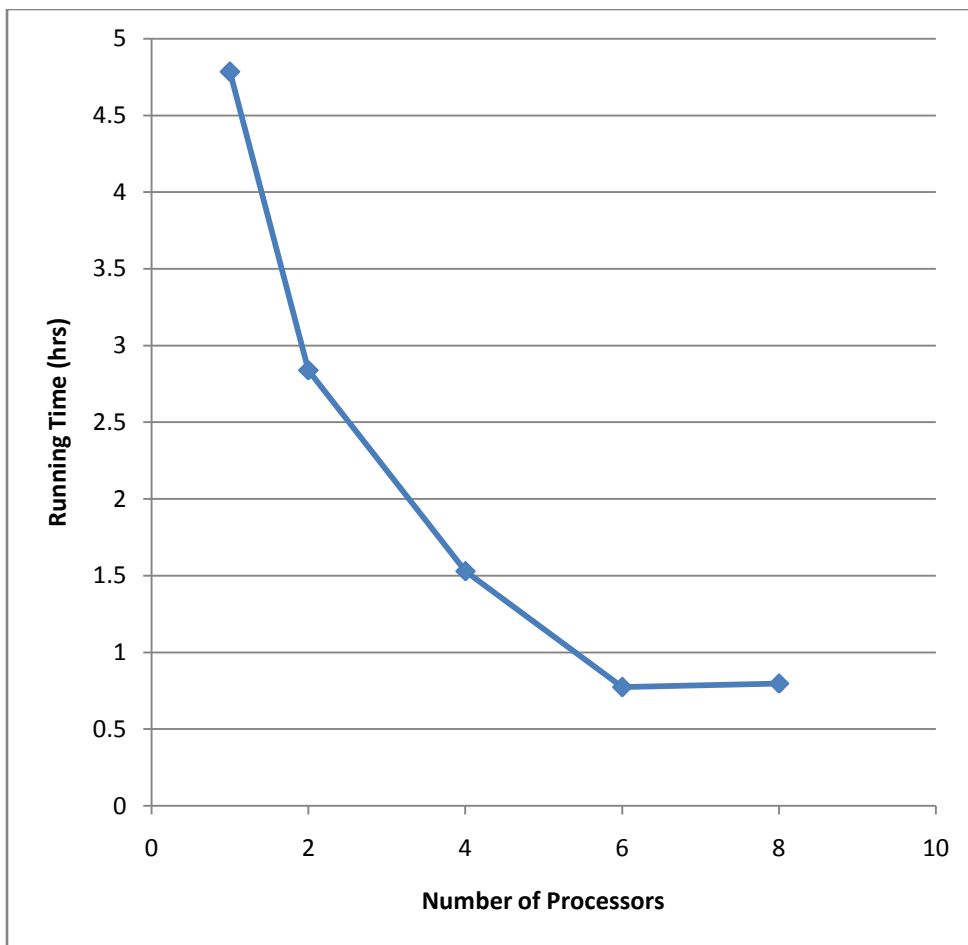
(b)the 200 x 50 x 100 grid

Figure 8. A comparison of the serial and parallel implementation using different number of processors on different grids (cont.)
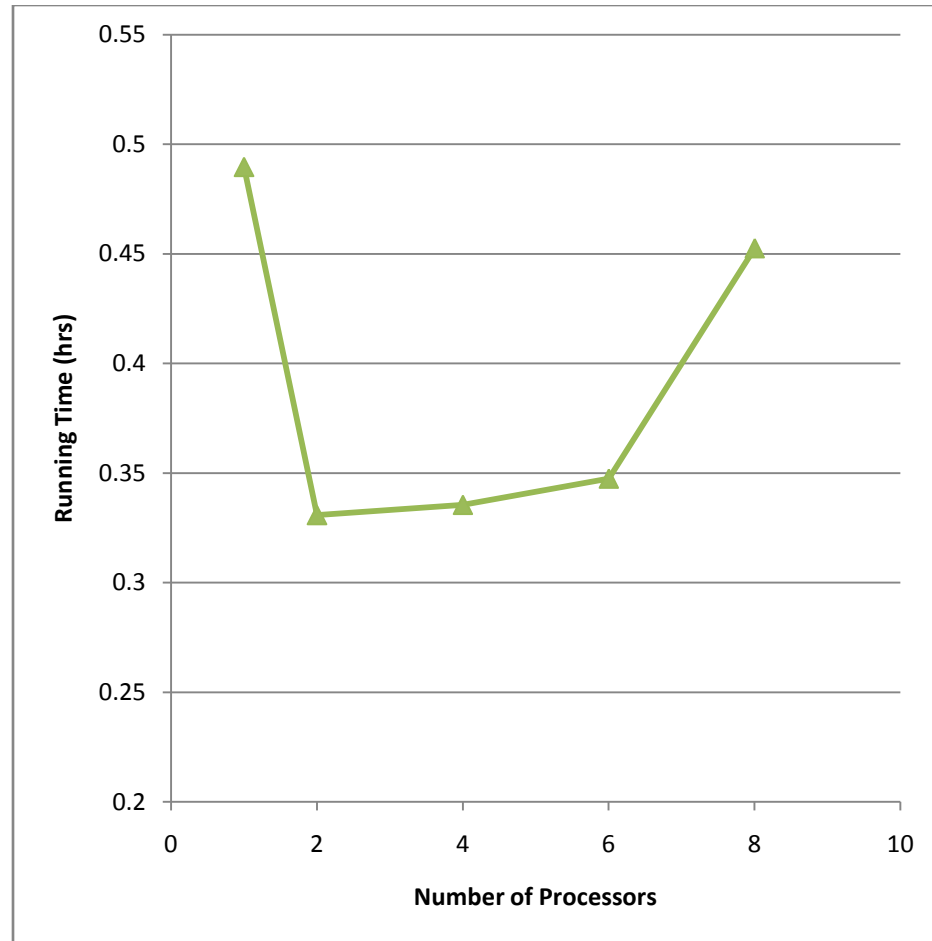
(c)the 100 x 25 x 50 grid

Figure 8. A comparison of the serial and parallel implementation using different number of processors on different grids (cont.)

From Figure 8(a), it is obvious that the more the number of processors, the less the computation time. Figure 8(a) also shows by how much the computation time reduces as the number of processors increases. It is expected that when the number of processors is doubled, the overall computation time is halved. However, this is not evident from the results. Take the 300 x 75 x 150 grid for instance, when the number of processors is

doubled from 1 to2, the computation time is reduced from 13.27 hours to 7.92 hours

respectively. The 16.2% loss in computation time is attributed to the communication

among the processors.

From Figure 8(b), it can be deduced that for a given calculation domain, there is

an optimal number of processors to use in order to maximize utilization of the parallel

implementation. On the 200 x 50 x 100 grid, using 8 processors requires a longer

computation time than using 6 processors although the reverse is expected. The increase

in the computation time is attributed to the excessive exchange of data among the

processors. For Figure 8(c), on the 100 x 25 x 50 grid, it can be seen that using only 2

processors takes the shortest computation time because of the same reason. It can

therefore be concluded that the optimal number of processors is a function of the domain

size.

4. CONCLUSIONS

A self-consistent laser deposition model is presented, which simulates heat

transfer, fluid flow, melt pool geometry during the laser deposition process. The *ICCG*

solver adopted to track the evolution of the melt pool free surface (liquid/vapor interface).

The continuum model [12, 13] is applied to derive the mass, momentum and energy

conversation equations, which are valid for solid and liquid. The movement of

solid/liquid interfaces are also simulated using the continuum model[12, 13]. In this

study, processes associated with the melt pool free surface, including free surface

evolution, convection, evaporation, surface tension, heating of powder particles, powder flow velocities, and powder concentration distribution have been modeled.

The numerical model is used to predict the deposition profile and the temperature field in Ti-6Al-4V by both sequential and the parallel implementations. The differences between the sequential and parallel implementations have also been analyzed. Therefore, it becomes very useful when trying to model with finer mesh for good accuracy of the simulation results. However, for each domain size, there is the optimal number of processors to use when simulating with the parallel implementation.

5. ACKNOWLEDGEMENTS

6. RERERENCES

1. R.R. Unocic and J.N. DuPont, "Composition Control in the Direct Laser-Deposition Process," *Metallurgical and Materials Transactions B*. Vol. 34B, no. 8, pp. 439-, 2003.

2. H. Gedda, A. Kaplan, and J. Powell, "Melt-Solid Interactions in Laser Cladding and Laser Casting," *Metallurgical and Materials Transactions B*. Vol. 36B, no.10, pp.683-, 2005.

3. T. C. Lei, J. H. Ouyang, Y. T. Pei, and Y. Zhou, "Microstructure and Sliding Wear Properties of Laser Clad TiN reinforced Composite Coating," Surface Engineering, vol. 12 no. 1 pp.55-60, 1996.

4. A. F. H. Kaplan and G. Groboth, "Process Analysis of Laser BeamCladding," *Journal of Manufacturing Science and Engineering (Transactions of the ASME)*, USA, Vol. 123, no. 4, pp. 609-614, Nov. 2001.

5. K. G. Watkins, "Achieving the Potential of Direct Fabrication with Lasers," *Proc 3rd International Conference on Laser Asssisted Net Shaping (LANE 2001) Erlangen*, 28-31 August, 2001,pp 25-38 Meisenbach- Verlag Bamberg.

6. M. L. Griffith, Materials and Design, vol. 20, pp. 107-113, 1999.

7. W. Hofmeister, JOM, vol. 51, no.7, 1999.

8. A. Vasinonta, J. Beuth, and M. Griffith, Proceedings of the Solid Freeform Fabrication Symposium, Austin, TX, pp. 383-391, 1999.

9. C. A. Brice, K. I. Schwendner, D. W. Mahaffey, E. H. Moor, and H. L. Fraser, Proceedings of the Solid Freeform Fabrication Symposium, Austin, TX, pp. 369-374, 1999.

10. J. Brooks, C. Robino, T. Headley, S. Goods, and M. Griffith, Proceedings of the Solid Freeform Fabrication Symposium, Austin, TX, pp. 375-382,1999.

11. A.G. Blake, and G.M.Eboo,"State of the Art Laser Hardfacing Using Dynamic Powder Feed Technology, "Conference on the Laser vs. the Electron Beam in Welding, Cutting and Surface Treatment, Reno, Nevada, pp. 196-214, 1985.

12. W. Bennon and F. Incropera, International Journal of Heat and Mass Transfer, vol. 30, pp. 2161-70, 1987.

13. W. Bennon and F. Incropera, International Journal of Heat and Mass Transfer , vol. 30, pp. 2171-87, 1987.

14. C.R.Swanminathan and V.R.Voller, "A General Enthalpy Method for Modeling Solidification Process," Metallurgical Transactions B(USA). Vol. 23B, no. 5, pp.651-664. Oct. 1992.

15. C. Prakash and V. Voller, Numerical Heat Transfer, vol.15B, pp171-89, 1989

16. S. Asai and I. Muchi, Trans. Iron Steel Inst. Jpn., vol. 18, pp. 90-98, 1978.

17. T. E. Sparks and Z. Fan, measurement of laser absorption coefficient of several alloys for diode laser, unpublished report, 2006.

18. A. Frenk, M. Vandyoussefi, J. Wagniere, A. Zryd, and W. Kurz Metall. Mater. Trans. B, 1997,vol. 28B, pp. 501-07.

19. M. Choi, R. Greif and M. Salcudean, Numerical Heat Transfer, vol. 11, pp477-489, 1987.

20. B. van Leer (1979), Towards the Ultimate Conservative Difference Scheme, V. A Second Order Sequel to Godunov's Method, J. Com. Phys., 32, 1979, pp. 101–136.

21. A.J. Chorin (1968), Numerical solution of the Navier-Stokes equations, Mathematics of Computation, Vol. 22, No. 104, (October 1968), pp. 745-762, ISSN 0025-5718.

22. D. S. Kershaw (1978), The incomplete cholesky-conjugate gradient method for iterative solution of systems of linear equations, J Comp Phys (1978),Vol.26, pp. 43-65.

23. D. A. Knoll, D. B. Kothe and B. Lally (1999), A new nonlinear solution method for phase change problems, Numerical Heat Transfer, Part B Fundamentals, Vol. 35, No. 4, (December 1999), pp. 436–459, ISSN 1040-7790.

24. D. Gueyffier, J. Li, A.Nadim, R. Scardovelli and S.Zaleski (1999), Volume of Fluid interface tracking with smoothed surface stress methods for three-dimensional flows. Journalof Computational Physics, Vol. 152, No.2, (July 1999), pp. 423-456, ISSN 0021-9991.

25. R. Scardovelli and S. Zaleski (2000), Analytical relations connecting linear interfaces and volume fractions in rectangular grids, Journal of Computational Physics, Vol. 164, No.1, (October 2000), pp. 228-237, ISSN 0021-9991.

26. R. Scardovelli and S. Zaleski (2003), Interface Reconstruction with Least-Square Fit and Split Eulerian-LagrangianAdvection.International Journal for Numerical Methods in Fluids, Vol. 41, No.3, (January 2003), pp. 251-274, ISSN 0271-2091.

27. B. Barney, Lawrence Livermore National Laboratory. "Message Passing Interface (*MPI*)." Internet:https://computing.llnl.gov/tutorials/mpi/, Oct 29, 2013l.

28. HPCVL and Compute Canada Workshop. "Introduction to High Performance Computingat the High-Performance Computing Virtual Laboratory." Internet: http://www.hpcvl.org/, Oct 29, 2013.

29. University of Tennessee, Knoxville, Tennessee. "MPI: A Message-Passing Interface Standard." Internet: http://www.mpi-forum.org/docs/mpi-1.1/mpi-11-html/mpi-report.html#Node0, Oct 29, 2013.

30. Indiana University, Bloomington, IN, USA. "Open MPI: Open Source High Performance Computing." Internet: http://www.open-mpi.org/, Oct 29, 2013

31. Todd E. Sparks and Zhiqiang Fan, measurement of laser absorption coefficient of several alloys for diode laser, unpublished report, 2006.

32. S.M. Kelly, "Thermal and Microstructure Modeling of Metal Deposition Processes with Application to Ti-6Al-4V", Ph.D. thesis, Virginia Polytechnic Institute and StateUniversity, 2004.

33. 30. K. C. Mills, "Recommended values of thermophysical properties for selected commercial alloys," Woodhead, Cambridge, 2002.

34. 31. Tobias Lips and Bent Fritsche, "A COMPARISON OF COMMONLY USED RE-ENTRY ANALYSIS TOOLS", 55th International Astronautical Congress 2004 - Vancouver, Canada IAC-04-IAA.5.12.2.09, P.9, SCARAB model.

SECTION

2. CONCLUSIONS

A self-consistent three-dimensional model was developed for the laser metal deposition process by powder injection, which simulates heat transfer, phase changes, and fluid flow in the melt pool. The continuum model was adopted to deal with different phases in the calculation domain.

The governing equations used in the model were discretized in the physical space using the finite volume method. The fluid flow and energy equations were solved in a coupled manner. The incompressible flow equations were solved using a two-step projection method, which requires a solution of a Poisson equation for the pressure field. The discretized pressure Poisson equation was solved using the Incomplete Cholesky Conjugate Gradient (*ICCG*) solution technique. The energy equation was solved by an enthalpy-based method. Temperature-dependent thermal-physical material properties were considered in the numerical implementation.

The numerical model, used to predict the deposition profile and the temperature field in Ti-6Al-4V by both sequential and the parallel implementations, has been presented. The differences between the sequential and parallel implementations have also been analyzed. Therefore, it becomes very useful when trying to model with finer mesh for good accuracy of the simulation results. However, for each domain size, there is the optimal number of processors to use when simulating with the parallel implementation.

VITA

Xueyang Chen was born in the city of Xiaogan, China. She obtained her Bachelor's Degree in Chemistry from University of Science and Technology of China (USTC), Hefei, China in 2011.

She enrolled in Missouri University of Science and Technology (Missouri S&T, formerly the University of Missouri - Rolla) in Manufacturing Engineering since2011 and worked as a Graduate Research Assistant under Dr. Frank Liou. She will receive her Master's Degree in Manufacturing Engineering at Missouri University of Science and Technology in December, 2013.